# CrystEngComm

Accepted Manuscript






ROYAL SOCIETY OF CHEMISTRY

www.rsc.org/crystengcomm

CyrstEngComm RSCPublishing

ARTICLE

# Porous Corundum-type $In_2O_3$ Nanoflowers: Controllable Synthesis, Enhanced Ethanol-sensing Properties and Response Mechanism

Cite this: DOI: 10.1039/x0xx00000x

Received 00th January 2012,
Accepted 00th January 2012

DOI: 10.1039/x0xx00000x

www.rsc.org/

Liping Gao,[†a] Fumin Ren,[† b] Zhixuan Cheng,[c] Yuan Zhang,[c] Qun Xiang,[c] and Jiaqiang Xu[*c,d]

Porous rhombohedra $In_2O_3$ (corundum-type $In_2O_3$, rh-$In_2O_3$) with the morphology of uniform nanoflowers was fabricated by using a mild, facile solvent-thermal method. The formation mechanism and transformation of phase were studied. The results revealed that the precursors were transformed from $In(OH)_3$ to InOOH with the increase of reaction time. The phase transformation were attribute to the stability of the InOOH phase at small crystal volume, less water molecules and small pH value, which in turn led to the formation of metastable rh-$In_2O_3$. The optimal working temperature of the sensor based on porous rh-$In_2O_3$ nanoflowers was proved to be 280 ℃, corresponding with chemisorbed oxygen analysis based on a temperature changeable XPS, further demonstrating the surface resistance controlled gas sensing mechanism of $In_2O_3$. The sensor exhibited an enhanced response and rapid response/recovery toward ethanol vapour, which was ascribed to hierarchical porous structure and more active defects.

## Introduction

In the past few years, many efforts have been devoted to control the structure and morphology of $In_2O_3$ to improve their sensing properties. Various $In_2O_3$ nanostructures, such as nanoparticles,[1] nanocubes,[2] nanowires,[3,4] nanobelts,[5] nanotubes,[6] nanofibers,[7] nanocrystal chains,[8] multipods[9] and some microstructure[10-12] have been successfully prepared by using either physical deposition or chemical methods. Recently, three-dimensional (3D) structure from nanobuilding blocks has attracted researchers' attention.[13-22]Furthermore, the research of precise control of nucleation, the growth process of the material and the phase transformation still remains a challenge. 3D $In_2O_3$ nanostructures have been reported by some researchers, but most of them were in cubic lattice. $In_2O_3$ nanomaterials with corundum structure (rh-$In_2O_3$) are rarely studied. Previously, rh-$In_2O_3$ was prepared through a phase transition method at high temperature and pressure.[23] Some research groups[24, 25]have successfully synthesized 3D rh-$In_2O_3$ with solvothermal method, the size of obtained products were relative large. It was well known that [26] the smaller particles have larger specific area, which would bring better gas response for surface resistance controlled gas sensor. Therefore, synthesizing small 3D nanostructure materials by controlling crystal growth and self-assembly may be not only a better choice for improving the performance of $In_2O_3$ gas sensors, but also a challenge for synthesis of other materials.

The stable phase of $In_2O_3$ is a body centered cubic bixbyite type crystal structure (bcc-$In_2O_3$, $Ia\bar{3}$), and the metastable corundum type $In_2O_3$ is a rhombohedral structure (rh-$In_2O_3$, $R\bar{3}c$). It has been verified that the formation of InOOH is a key step for obtaining rh-$In_2O_3$.[27,28]The presence of $In(OH)_3$, on the other hand, were suggested to promote the formation of c-$In_2O_3$.[27] Lin et al[29] reported that InOOH phase appeared to be formed before the $In(OH)_3$ phase in aqueous solution. So, adopting appropriate reaction condition could controllably synthesize different crystal structure of the product. Previous works[30, 31] revealed that for $In_2O_3$ nanocrystals, an increase in the reaction time caused the increase in the fraction of large NCs under their conditions due to an increase in the rate of phase transformation from rh-$In_2O_3$ to bcc-$In_2O_3$. However,

[a]Department of Physics, College of Science, Shanghai University, Shanghai, 200444, China
[b]Municipal engineering, Civil Engineering & Architecture, Beijing Jiaotong University, Beijing, 100081, Chinc
[c]NEST Lab, Department of Chemistry, College of Science, ShanghaiUniversity, Shanghai, 200444, China.E-mail:xujiaqiang@shu.edu.cn; Tel: +86 21 66132701
[d]State Key Laboratory of Transducer Technology, Shanghai Institute of Microsystem and Information Technology, Chinese Academy of Sciences, Shanghai, 200050, China
Electronic Supplementary Information (ESI) available: See DOI:10.1039/b000000x

they also demonstrated that rh-$In_2O_3$ NCs were stable when the size was smaller than 5 nm under applied conditions. The stabilization of metastable corundum-type $In_2O_3$ has been achieved by the conversion of bcc-$In_2O_3$ at high pressures and temperatures.[23, 32] However, the pathway from In $(OH)_3$ to InOOH by doping was also discussed in the literatures, [33, 34] which was another method for the transformation from bcc-$In_2O_3$ to rh-$In_2O_3$. To the best of our knowledge, the direct investigation of the phase transformation from bcc-$In_2O_3$ to rh-$In_2O_3$ by changing the reaction time has not been reported.

In this paper, porous rh-$In_2O_3$ nanoflowers were synthesized by annealing flower-like InOOH precursor at 500 ℃. The morphology and phase transformations of $In_2O_3$ during their growth in solution were also investigated. Comparing with other morphologies obtained at different reaction time, the porous rh-$In_2O_3$ nanoflowers exhibited enhanced sensing properties toward ethanol. Corresponding gas-sensing mechanism were speculated based on gas sensing tests, XPS and PL spectrum.

## Experimental

**Synthesis:** The reagents were all purchased from Sinopharm Chemical Reagent Co., Ltd. (Shanghai, China) and used without further purification. In a typical synthesis, 6mL In $(NO_3)_3 \cdot 5H_2O$ (0.10 M) aqueous solution, 20 mL glycol and 13 mL ethanol solution were mixed together, and then 0.2 g PVP was added into the solution. The mixture was transferred into a Teflon-lined stainless steel autoclave of 50 mL capacity. The autoclave was sealed and maintained at 180 □ for 24 h, and then naturally cooled down to room temperature. Finally the white precipitate was collected, centrifuged and washed several times with distilled water and absolute ethanol alternatively, followed by dried at 60 □ for 4 h to obtain the precursor InOOH. To obtain rh-$In_2O_3$, the precursor was put into a quartz crucible and annealed in a muffle furnace at 500 □ for 2 h. Different reaction system were involved in this paper. By changing the solvent, different phase and morphology $In_2O_3$ can be obtained. In $H_2O$ system, 33 mL $H_2O$ were used as reaction solvent. In ethanol system, the solvent of $H_2O$ was replaced by ethanol. In ethanol and glycol system, part ethanol was replaced by glycol, and the volume of ethanol and glycol were 20 mL and 13 mL, respectively.

**Characterization:** Powder X-ray diffraction was performed with a DX-2700 and Rigaku D-MAX/ IIAX-ray diffactometer at a rate of 1.8° (2θ)/min with Cu Kα radiation. Scanning electron microscopy (SEM) (JSM-6700F) and transmission electron microscope (TEM) (JEM-2010F) were employed to observe the morphology of prepared materials. The decomposition process of the precursors was investigated on a STA499C thermal analyzer (Netzsch, Germany) with a heating rate of 10 ℃ $min^{-1}$ under $N_2$ atmosphere. The $N_2$ adsorption-desorption analyses were carried out at liquid nitrogen temperature on an ASAP 2020 analyzer (Micromeritics Instrument, USA).The XPS data were recorded at different temperature on an ESCALAB 250 Xi XPS system of Thermo Fisher Scientific, England and excited by monochromatic Al Ka radiation. The peak at 284.6 eV attributed to the C–C band in the C1s spectrum was used for binding energy reference. Room temperature photoluminescence (PL) measurements were conducted on a Hitachi RF-5301PC spectrofluophotometer by using 325 nm Xe laser line as an excitation source.

**Sensor fabrication and gas response test:** Fig. 1 is a schematic of the sensor structures, in which a pair of Au electrodes was printed previously on both sides of the alumina ceramic tube, while a Ni-Cr wire heater inside of the ceramic tube was used to control the working temperature of the sensor. The fabrication of side-heated gas sensor was described as follows. Firstly, the samples were mixed and ground with an adhesive in an agate mortar to form a gas sensing paste. Then, the paste was coated on an alumina ceramic tube located among the two Au electrodes, and dried under IR radiation for 15 min. Subsequently the alumina ceramic tube was sintered at 500 ℃ for 2 h, and then welded onto a pedestal. Finally, the obtained sensors were aged at 300 ℃ for 7 days for increasing their stability.

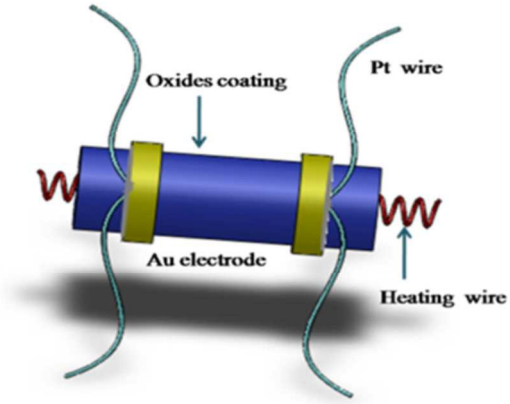


Fig.1 Sketch of the gas-sensor structure

The test was operated in a measuring system of HW-30A (Hanwei Electronics Co. Ltd., P.R. China). A stationary state gas distribution method was used for testing gas response. In this measurement, the humidity is controlled within the range of 40–50% RH. The gas response of the sensor in this paper was defined as $S = R_a/R_g$ (reducing gases) or $S = R_g/R_a$ (oxidizing gases), where $R_a$ and $R_g$ were the resistance in air and test gas, respectively. The response or recovery time was expressed as the time taken for the sensor output to reach 90% of its saturation after applying or switching off the gas in a step function.[35, 36]

## Results and discussion

### Synthesis, crystal phase and morphology evolution of $In_2O_3$

Fig. 2(a1) showed the powder X-ray diffraction (XRD) pattern of the precursor. All the peaks can be indexed to InOOH with an orthorhombic phase. XRD pattern of the product annealed at

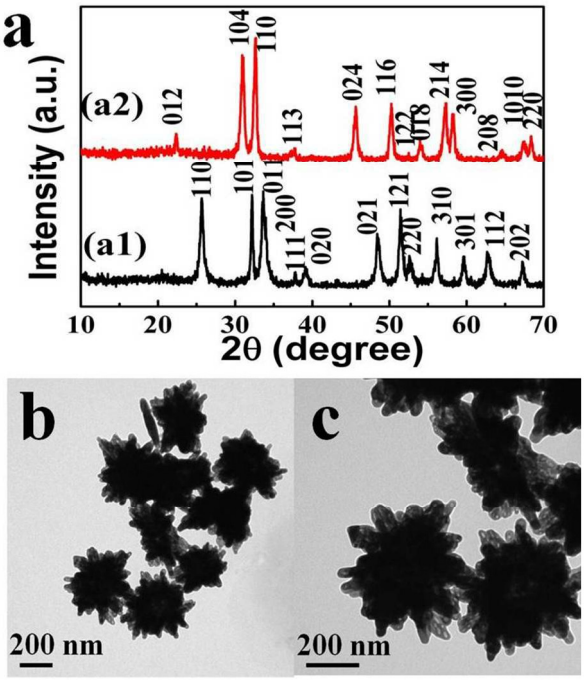


Fig.2 (a) XRD patterns of the InOOH precursors (a1) and the porous $In_2O_3$ nanoflowers (a2), (b) TEM image of InOOH and (c) TEM image of the porous $In_2O_3$ nanoflowers.

500 ℃ was displayed in Fig. 2(a2). All the peaks in the pattern were consistent with a JCPDS Card of No. 73–1809, indicating the successful synthesis of the hexagonal $In_2O_3$ phase (rh-$In_2O_3$) under a mild reaction condition. The morphology of InOOH and $In_2O_3$ were observed by TEM. Fig. 2b showed a typical TEM image of the InOOH sample. It could be found that the diameter of InOOH nanoflowers was about 400–600 nm. Obviously, the nanoflowers are assembled by a number of porous nanorods and small nanosheets. A higher magnification TEM image (Fig. 2c) revealed more direct information about the morphology of the synthesized $In_2O_3$. It could be found that the flower-like nanostructure can be maintained after calcinations. The pores with size below 30 nm existed on the nanorods and nanosheets can be clearly seen.

XRD patterns and SEM images of the products synthesized by using different solvents were shown in Fig. 3

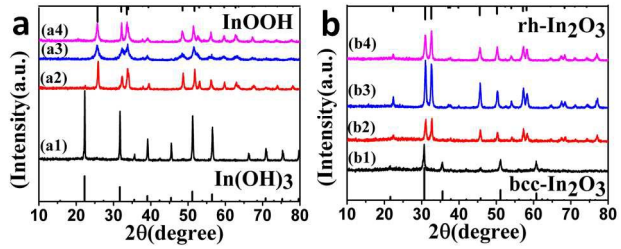


Fig.3 XRD patterns of the precursors and products using different solvent, (a1and b1) $H_2O$, (a2 and b2) ethanol, (a3 and b3) ethanol and glycol, (a4 and b4) ethanol, glycol and PVP.

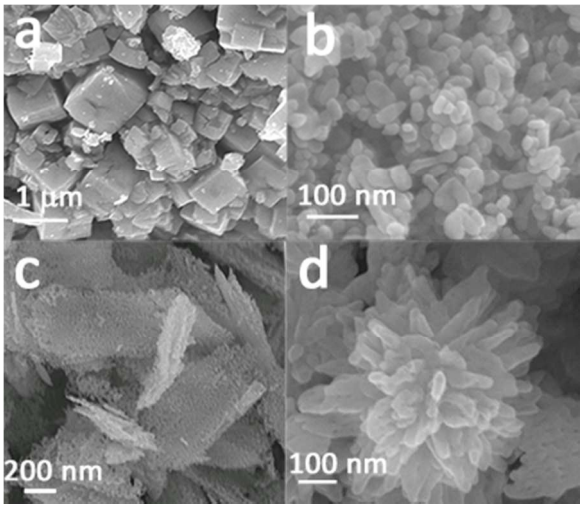


Fig.4 SEM images of $In_2O_3$ using different solvent, (a) $H_2O$, (b) ethanol, (c) ethanol and glycol, (d) ethanol, glycol and PVP.

and Fig. 4. While in $H_2O$ system, In $(OH)_3$ and bcc-$In_2O_3$ can be obtained (Fig. 3a1 and Fig. 3b1), and bcc-$In_2O_3$ nanorectangles can be observed clearly (Fig.4a). In the system of ethanol and the system of part ethanol replaced by glycol, peaks in the XRD patterns were indexed to InOOH and hexagonal $In_2O_3$ phase (Fig. 3a and Fig. 3b), and nanoparticles and nanosheets could be obtained from Fig.4b and Fig.4c. The reason for the different morphology may be resulted from $In^{3+}$ combination with ethanol units through the formation of In—O—covalent and In—OH coordination bonds. However, ethanol is a small molecule solvent with one –OH, which promotes the formation of nanoparticles. When ethanol was partly replaced by glycol, $In^{3+}$ combined with glycol and ethanol unit, leading to the formation of longer chains, due to glycol underwent several steps of intermediate reactions to form longer chains as described in previous literature. [37] Finally the long chains could further self-assembled into nanosheets through van der Waals interactions. PVP has been widely used as a capping agent and surfactant in controlling the growth and structure of some ceramic and metal oxide. It was employed as morphology control agent to synthesize different morphology and structure of $In_2O_3$ by hydrothermal method [38]. Porous nanoflowers assembled by nanosheets and nanorods (Fig. 4d) can be obtained by using ethanol and glycol as solvent, and PVP as the surfactant. The role of PVP was to promote the assembling of nanosheets and nanorods into nanoflowers.

To study the effect of surfactants on morphology, cetyltrimethyl ammonium bromide (CTAB), a cationic surfactant, was added into the reaction system. The results showed that CTAB could not make product assemble effectively, on the contrary, make the product decompose into nanoparticles, as shown in ESI (Fig.1s).

To investigate the morphology evolution and formation mechanism of $In_2O_3$ nanoflowers, their growth processes were followed by examining the products collected at different reaction time. At ambient pressure, only bccc-$In_2O_3$ could be

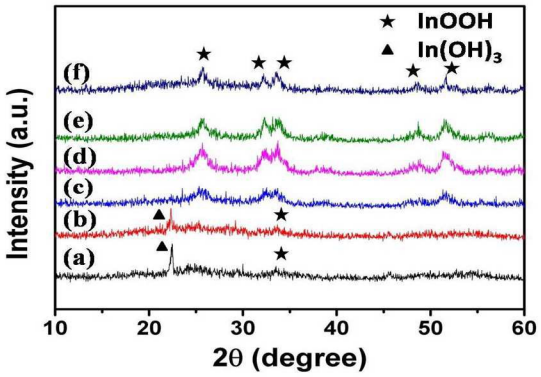


**Fig.5** XRD patterns of the precursors obtained after different growth stages: (a) 0.5 h, (b) 1 h, (c) 3 h, (d) 6 h, (e) 12 h and (f) 24 h.

obtained through thermal dehydration of $In(OH)_3$,[39] whereas, the thermal decomposition of InOOH could lead to the formation of rh-$In_2O_3$.[40] The reaction during this process could be suggested as following:

$$In^{3+} + 3H_2O \rightarrow In(OH)_3 + 3H^+ \quad (1)$$

$$In(OH)_3 \rightarrow InOOH + H_2O \quad (2)$$

$$2In(OH)_3 \rightarrow c\text{-}In_2O_3 + 3H_2O \quad (3)$$

$$2InOOH \rightarrow rh\text{-}In_2O_3 + H_2O \quad (4)$$

Thus，different precursors play a key role on the crystal phase of final product. XRD patterns of precursors collected at different times during the synthesis were shown in Fig.5. Obviously, a change in the crystal structure was observed during the reaction. At the early stage, the XRD pattern was in good agreement with cubic $In(OH)_3$ phase, and the small amounts orthorhombic InOOH phase was existent, which was consistent with previous references.[29,41] As the reaction proceeds, the peaks corresponding to InOOH became apparent.

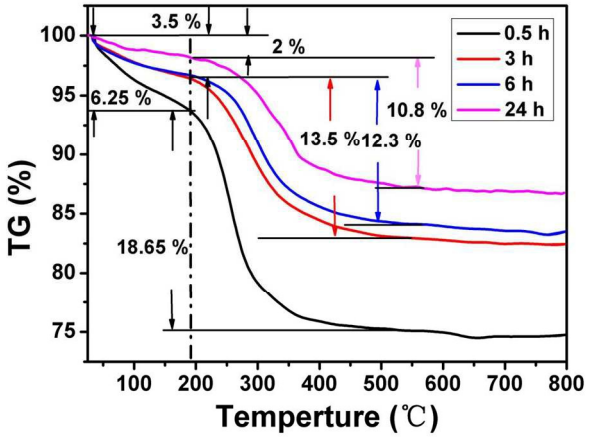


**Fig.6** TG curves of the precursors obtained at different stage.

These peaks were significantly broader than the peaks corresponding to $In(OH)_3$, indicating the change from cubic to orthorhombic.[31] With the increase of reaction time, the broadening of XRD peaks decreased (Fig.5e, Fig. 5f) due to the growth of crystal.

TG analysis was carried out to examine the conversion process of the precursors during calcinations. Fig. 6 was the TG analysis of the precursor prepared at four different growth stages. The total weight loss of 24.9%, 17%, 15.8% and 12.8% (40℃ to 600℃) were shown in TG curves, respectively. The weight losses from 40 to 200 □ were attributed to the removal of existing adsorbed water and glycol in the precursors. The theory weight loss of In $(OH)_3$ and InOOH to $In_2O_3$ are calculated as 16.28% and 6.08%, respectively. For the precursor obtained after 0.5 h, the weight loss of the second step from 200 to 600□ was ca. 18.65%. However, from the XRD pattern (Fig.4a), the product was composed of $In(OH)_3$ and InOOH, and the redundant weight loss compared with theoretical value indicated that some other species were decomposed. A possible speculation was that the redundant weight loss was attributed to the removal of existing adsorbed PVP in the precursors. Assuming the amount of PVP was certain on every pattern, the weight lose was on the decrease from the second step, indicting the increase of InOOH phase, which accorded with the XRD analysis from Fig.5.

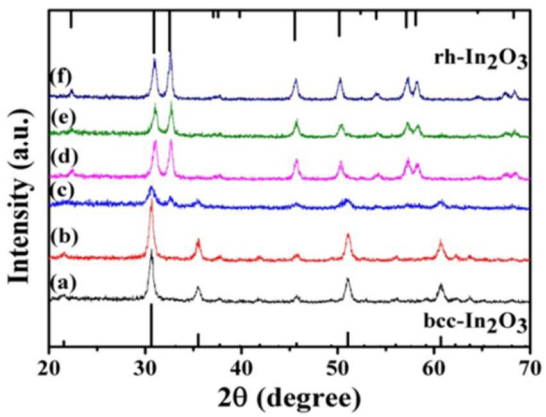


**Fig.7** XRD patterns of $In_2O_3$ obtained after different growth stages: (a) 0.5 h, (b) 1 h, (c) 3 h, (d) 6 h, (e) 12 h and (f) 24 h.

Fig.7 displayed the XRD patterns of the products obtained by annealing precursors at 500℃ for 2 h. The changes of the crystal structure were shown clearly. With the increasing of reaction time, a decrease of bcc-$In_2O_3$ and an increase of rh-$In_2O_3$ could be observed, corresponding with the transformation from In $(OH)_3$ to InOOH (Fig.5).

In the process of reaction, the phase of product transformed from bcc-$In_2O_3$ to rh-$In_2O_3$, however, whether the morphology of product would be changed? In this paper, we studied the morphology of products under different reaction time (Fig. 8). At the early stage, spindle type nanorods were formed (Fig. 8a, 8b). A similar result can be found by Avivi et al, [42] who reported the nano-sized needle-shaped $In(OH)_3$ particles prepared via the sonication of an aqueous solution of

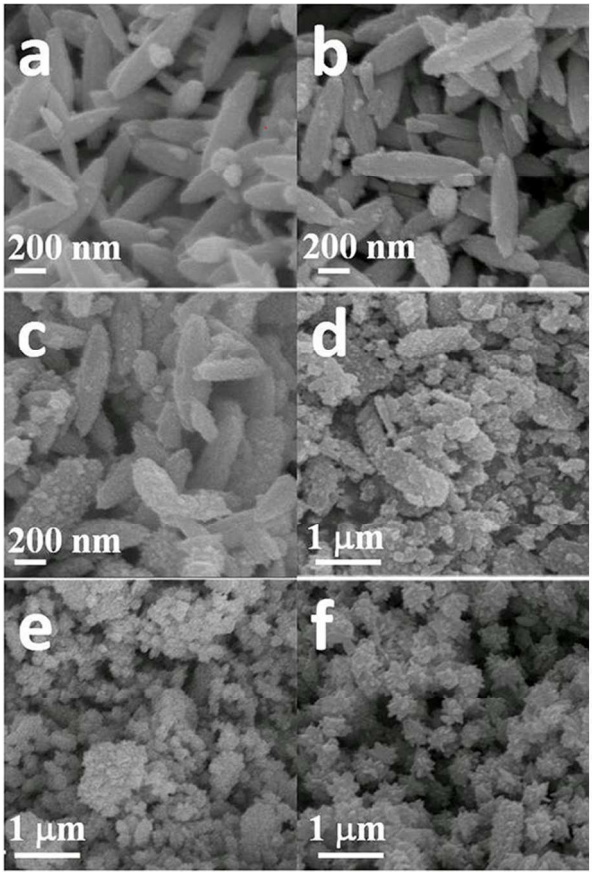


Fig.8 SEM images of the $In_2O_3$ obtained at different growth stages: (a) 0.5 h, (b) 1 h, (c) 3 h, (d) 6 h, (e) 12 h and (f) 24 h.

$InCl_3$. As is known, bcc-$In_2O_3$ could be obtained by the thermal dehydration of $In(OH)_3$. When the reaction time was extended to 3 h, the characteristic peak of rh-$In_2O_3$ appeared obviously (Fig.7c). The morphology was confirmed as nanosheets, which was assembled from small nanoparticles (Fig.8c). Previous work[31] reported that a decrease in the growth rate would lead to formation of small NCs and the stabilization of rh-$In_2O_3$. So, we hypothesized that the nanosheets were assembled by some small rh-$In_2O_3$ nanoparticles. As the reaction proceeded to 6 h, the spindle type nanorods had almost disappeared and a large amount of nanosheets assembled by nanoparticles can be obtained (Fig. 8d). After 12 h, the size of some nanosheets decreased and small nanoflowers appeared, as shown in Fig. 8e. As the aging process continued, nanoflowers assembled by nanorods and nanosheets successfully were obtained (Fig.8f). In this process, the small nanoflowers grew to large nanoflowers via the Ostwald ripening process.

Water-free synthesis in non-basic organic solvents did not yield any NCs.[31] For this reason, controlling the presence of small amounts $H_2O$ in solution was needed for the formation of $In(OH)_3$and InOOH by hydrolysis. A small amount of water in our reaction system can promote the formation of rh-$In_2O_3$, however, when the reaction system contained more water, bcc-$In_2O_3$ phase was synthesized (shown in Fig.3). As is known, pH value was also a factor to affect the phase of the final product. Under the pH value of 4～5 in our system, rh-$In_2O_3$ can be obtained. However, through adding NaOH to the system (pH ≈ 8), bcc-$In_2O_3$ phase can be obtained, as shown in ESI (Fig.2s).

It is known that the initial crystal nucleus is $In(OH)_3$ units in the presence of water solution. From our experiments, it became evident that the InOOH phase was present at short reaction times, which was in accord with the results obtained by Lin et al.[29] The formation of InOOH can be described as the obtained $In(OH)_3$ nuclei eliminating water molecules from their core while maintaining a hydroxide shell because of the lower water/solid interface energy of InOOH[41]. In general, with the reaction proceed, InOOH particles could transform to $In(OH)_3$ by incorporation of water, and the particles can grow without restriction and frustration because of the regular cubic crystal structure. However, under our experiment condition, there was not enough water to generate with InOOH, and less $OH^-$in the solution (less water) to response with $In^{3+}$ due to the acidity of reaction solution was strong with the pH value of 4～5. So, the generated water will rapidly react with redundant $In^{3+}$ to form $In(OH)_3$. Similar to the initial stage, the obtained $In(OH)_3$ nuclei should eliminate water molecules from their core to form InOOH. In this cycle, as time goes on, more InOOH could be obtained by hydrolysis. Finally, rh-$In_2O_3$ can be obtained by calcinating InOOH under certain temperature.

**Gas-sensing properties**

As is well known, monitoring the concentrations of ethanol is necessary for health and safety. [43] In this paper, the gas-sensing properties of $In_2O_3$ sensors were studied by using the method mentioned above.

The resistance changing and responses of the gas sensor based on porous $In_2O_3$ nanoflowers toward 20 ppm ethanol were shown in Fig. 9a, which were tested at different temperatures ranging from 130 ℃ to 380℃. The resistance of

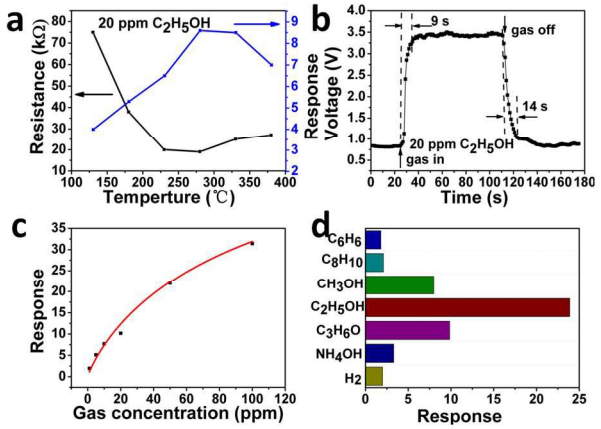


Fig.9 (a) Resistance versus operating temperature curves and ethanol gas sensing property of the sensor at different test temperatures, (b) Response curve of the sensor to 20 ppm ethanol, (c) Response of the sensor (S) vs. ethanol concentrations (C) and (d) Responses of the sensor to various gases (Concentration of all gases are 50 ppm).

**Table 1.** Influence of different reaction times on the response of sensor to 50 ppm ethanol.

| Reaction time | Phase | | Phase | | Morphology | BET surface areas ($m^2/g$) | Response to 50 ppm ethanol ($R_a/R_g$) |
|---|---|---|---|---|---|---|---|
| **0.5 h** | | | | | Nanorods | 18.6 | 16 |
| **1 h** | | | | | Nanorods | 18.8 | 16 |
| **3 h** | bcc-$In_2O_3$ | ↓ | rh-$In_2O_3$ | ↑ | Nanorods and nanosheets | 36.8 | 19 |
| **6 h** | | | | | Nanosheets and nanoparticles | 21.3 | 15 |
| **12 h** | | | | | Nanosheets and nanoflowers | 17.7 | 20 |
| **24 h** | | | | | Nanoflowers | 16.8 | 22 |

The direction of the arrow represents the decrease of the phase composition

the sensor decreased with the increasing of temperature (130℃ to 280 ℃), whereas increases when the temperature was above 280 ℃. The highest response can be gained at 280 ℃, which was in accord with the changing of resistance. Thus, the optimized 280℃ was chosen for further gas sensing tests of the $In_2O_3$ sensor. It is well-known that when bulk particles were exposed to a target gas, the gas only reacted with the outer surface of the particles, resulting in a poor response. If we use porous and hierarchical structure materials as gas sensing materials, the gas could diffuse into the interior space of these special structures, [38] increasing the surface utilization percentage, and further resulting in an enhanced response. Response dynamic curves of the sensor to 20 ppm ethanol were shown in Fig. 9b. It revealed that the response / recovery time of the sensor toward 20 ppm ethanol were less than 9 s and 14 s, respectively. Fig. 9c showed the response value of the sensor with the changing of ethanol concentration. The gas response (*S*) as a function of ethanol concentration ranging from 1-50 ppm (*C*) was well fitted by using the equation $S=abC/(1+bC)$, where a is the maximum adsorption amount and b is adsorption constant. This can be understood as the surface coverage of adsorbed molecules followed the Langmuir isotherm model, and the specific equation is showed as followed:

$$S = 53.577*0.014*C/(1+0.014*C),\ R^2=0.984 \quad (5)$$

At a lower concentration, the sensor exhibits a linear relation between the sensor response and ethanol concentration as shown in Fig.9c. At higher concentration, the surface coverage tends to saturate and hence leads to a saturation response. To check the selectivity of the sensor, we measured the responses to some other gases (50 ppm) including $C_6H_6$, $C_8H_{10}$, $CH_3OH$, $CH_3COCH_3$, $NH_4OH$ and $H_2$ at 280 ℃. As shown in Fig.9d, the response of the sensor to 50 ppm ethanol was about 22, which was at least two times more than other test gases.

In order to examine the influence of phase composition and morphology on the gas-sensing properties, surface areas of the samples and the response to 50 ppm ethanol under different reaction time were shown in Table 1. From the XRD and TG analysis of the products, it can be seen clearly that the rh-$In_2O_3$ became apparent with the increase of reaction time. Previous work[31] pointed out that the size of the particle became small with the emergence of rh-$In_2O_3$. At the reaction of 3 h, great changes have take place on the phase of the product (Fig.7). Therefore, in this stage, the product has the smaller particles and larger specific surface area (36.8$m^2$/g). The larger surface area promoted the improvement of the sensor to ethanol (0.5 h to 3 h). After the acute phase transition with the increase of reaction time, the material gradually stable in hexagonal phase, at the same time, self-assembled into new morphology (3 h to 24 h). In this process, the specific surface area of the product has a certain decrease, but the gas-sensing properties have a certain improvement. We considered the result was due to the

**Table 2.**The reported responses of different morphology $In_2O_3$ sensor to ethanol.

| | Ethanol Concentration(ppm) | WorkingTemperature (℃) | Response ($R_g/R_a$) | References |
|---|---|---|---|---|
| **$In_2O_3$nanoparticles** | 50 | 240 | ~5.5 | 44 |
| **$In_2O_3$nanorods** | 50 | 290 | ~7.5 | 45 |
| **$In_2O_3$nanoplates** | 100 | 150 | <5 | 46 |
| **$In_2O_3$hollow microspheres** | 50 | ~25(RT) | ~13 | 47 |
| **Lotus root slice-like$In_2O_3$microspheres** | 50 | 250 | <10 | 14 |
| **Flower-like$In_2O_3$hierarchical nanostructures** | 50 | 320 | <18 | 48 |
| **Porous rh-$In_2O_3$ nanoflowers** | 50 | 280 | 22 | This work |

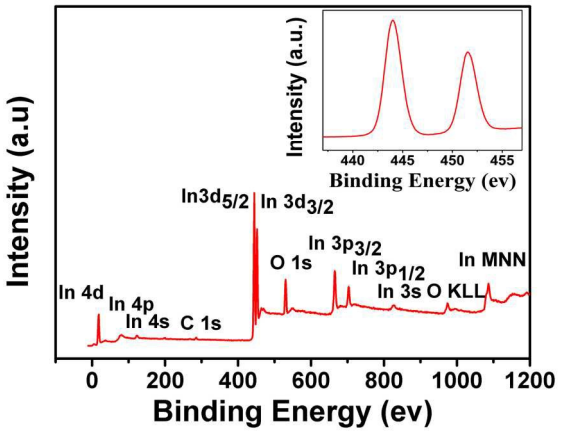


**Fig.10** XPS spectrum of porous rh-$In_2O_3$ nanoflowers at the test temperature of 25℃. The inset is the spectrum of In

combination of uniform morphology and the increase of hexagonal phase.

Table 2 showed the response of $In_2O_3$ sensors to ethanol reported previously. Obviously, the response of the porous rh-$In_2O_3$nanoflowes was much higher than those of $In_2O_3$nanoparticles, [44]nanorods, [45]nanoplates, [46]microspheres[14,47] and flower-like $In_2O_3$hierarchical nanostructures.[48] The gas sensing response enhancement may be attributed to small size 3D structure, porous structure and more active centers obtained from the enhanced oxygen vacancy defects on the porous nanostructure.

**Gas sensing mechanism**

For a surface resistance controlled gas sensor, such as $SnO_2$, ZnO or $In_2O_3$, chemisorbed oxygen on the surface of the sensing material plays key role in gas response. So we employed XPS to explore the adsorbed oxygen species on the material surface.

XPS of the porous rh-$In_2O_3$ nanoflowers at the temperature of 25 ℃ was shown in Fig. 10. It reveals that the sample is composed of In and O, and no visible impurities are detected, which was consistent with the XRD result. Fig. 10 showed that the peaks centred at ~ 451.58 and ~ 443.98 eV can be assigned to $In3d_{5/2}$ and $In3d_{3/2}$, and the peak centred at ~ 530.1 eV belong to the O1s. From XPS-peak-differenating analysis, we could clearly see that there were three peaks separately at ~529.4, ~530.5 and ~532.5eV (Fig. 11), which were attributed to three kinds of oxygen species on the surface of indium oxide. The first was lattice (surface) oxygen $O^{2-}$, the second was a dissociative type one $O^-$, together with molecular-type adsorbate $O_2^-$.Further studies indicated that the proportion of oxygen species changed with test temperature. Table 3 showed the atomic ratio of three kinds of oxygen species. At 280 ℃, $O^-$ in O1s spectra occupies more percentage compared with the one at other three temperatures. When the temperature was increased to 400 ℃, the atomic ratio of lattice (surface) oxygen $O^{2-}$ were greatly increased due to the conversion from other oxygen species as reported in the previous literature. [49] Since gas sensors are usually operated at rather high temperature (200–400 ℃), $O^-$ adsorbate, which is prior existence at about 300 ℃, is more important than the others. [35, 49]The result has been proved to be responsible for enhancing gas sensing of rh-$In_2O_3$ gas sensor, further helping us to understand the mechanism of gas sensing. XPS result was also a strong supporting evidence for the best working temperature (280 ℃) of the sensor.

**Table 3.** The proportion of oxygen species at different temperatures.

| Temperature (℃) / Atomic (%) | 25 | 150 | 280 | 400 |
|---|---|---|---|---|
| $O^{2-}$ | 57.69 | 76.23 | 63.58 | 83.96 |
| $O^-$ | 24.00 | 8.14 | 29.98 | 7.74 |
| $O_2^-$ | 18.31 | 15.64 | 6.44 | 6.44 |

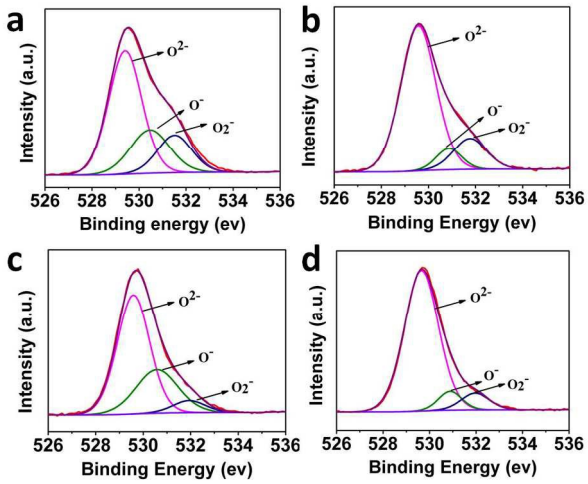


**Fig.11** O 1s spectrum of porous rh-$In_2O_3$ nanoflowers at different test temperature, (a) 25 ℃, (b) 150 ℃, (c) 280 ℃and (d) 400 ℃.

The resistances depending on working temperature of the sensors were investigated by measuring the resistance changes of the sensors. Once the $In_2O_3$ sensors exposed to air at certain temperature, oxygen molecules would adsorbed on the $In_2O_3$ surface, and trapped electrons from the conduction band to generate ionized oxygen species, such as $O_2^-$, $O^-$ and $O^{2-}$, resulting in an increase of the resistance for $In_2O_3$ sensor.[50,51] When upon exposed to a reducing gas, the gas could react with chemisorbed oxygen, and then return the electron back to the conduction band of the sensing material, decreasing the resistance of the sensor. Taking $C_2H_5OH$ as an example, it is proved to be converted to $CH_3CHO$ when $In_2O_3$ was used as the catalytic material under an alkalinity surface.[52] $CH_3CHO$ may react with the adsorbed oxygen ions on the sensor surface, meanwhile the trapped electrons would be given back to $In_2O_3$ causing the increase of electric conductivity. Thus, a possible

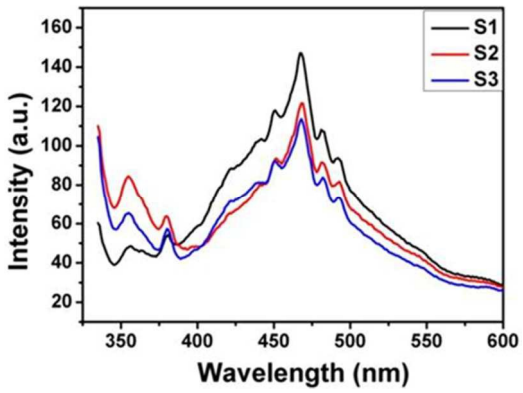


**Fig. 12** Photoluminescence spectra of different $In_2O_3$ samples at room temperature, λ ex= 325 nm.

mechanism for $In_2O_3$ response to ethanol was suggested as Eqn (1)-(6) in ESI.

Photoluminescence (PL) spectroscopy is a useful method to characterize the intrinsic and extrinsic defects in semiconductors. PL spectra of as-prepared $In_2O_3$ obtained at different reaction time were shown in Fig. 12. Porous rh-$In_2O_3$ nanoflowers sensor was labelled as S1 (Fig. 8f). Spindle type $In_2O_3$ nanorods (Fig. 8b) and $In_2O_3$ nanosheets/nanoparticles (Fig. 8d) sensors were labelled as S2 and S3, respectively. All the samples displayed strong UV emission at about 360 nm and 380 nm, which might be the characteristic near band-edge emission of the wide band gap from the recombination of the free excitons.[53] The emission peak positions from 450 nm to 490 nm for the samples were consistent with previous reference.[10] The different emission peaks were related to the different energy levels produced by the oxygen vacancies. Defects at metal oxide surfaces are believed to significantly influence the surface properties, such as heterogeneous catalysis, corrosion inhibition and gas sensing.[31] For S1, the blue-green light emissions were much stronger than the others, implying more structural defects existence, especially oxygen vacancies.[36] The existence of the oxygen vacancies was beneficial for oxygen adsorption, and in turn enhanced the chance of interaction with testing gases.[54, 55] PL analyses verified the result of Fig.3s in ESI that the S1 sensor based on porous rh-$In_2O_3$ nanoflowers obtained more oxygen adsorption and resulting in higher gas response.

## Conclusions

In this paper, porous rh-$In_2O_3$ nanoflowers were successfully synthesized by a facile solvent-thermal method. The factors influencing material morphology and crystal structure, such as solvent, surfactant, pH value and reaction time were studied in detail. With the increase of the reaction time, $In(OH)_3$ gradually transform to InOOH, which in turn promotes the formation of rh-$In_2O_3$. Gas-sensing properties detection of ethanol vapor indicated that the sensor based on porous rh-$In_2O_3$ nanoflowers with rational micro/nanostructure and point defects had high gas response, good selectivity and rapid response. The analysis based on X-ray photoelectron spectrum and the curves of gas response vs working temperature revealed that the best operating temperature of the sensor was at 280 ℃, suggesting its gas sensing mechanism is a surface resistance controlled mode. The response of the sensor to 50 ppm ethanol reached about 22, which was at least two times more than other test gases. The response and recovery time for the sensor to 20 ppm ethanol were less than 9 s and 14 s, respectively. The sensor based on porous rh-$In_2O_3$ nanoflowers exhibited excellent gas sensing performance toward ethanol, suggesting that the sensor has certain superiority in the selective detection of ethanol.

## Acknowledgements

This work was supported by National Natural Science Foundation of China (No. 61371021, 51301101).The authors thank the help of Instrumental Analysis and Research Center in Shanghai University for material characterization.

## Author information

Corresponding Author
xujiaqiang@shu.edu.cn
Author Contributions
†These authors contributed equally.
Notes
The authors declare no competing financial interest.

## References

1 N. Pinna, G. Garnweitner, M. Antonietti, M. Niederberger,, *J. Am. Chem. Soc.*, 2005, **127**, 5608.
2 X. H. Liu, L. B. Zhou, R. Yi, N. Zhang, R. R. Shi, G. H. Gao, G. Z. Qiu, *J. Phys. Chem. C*, 2008, **112**, 18426.
3 C. Li, D. H. Zhang, S. Han, X. L. Liu, T. Tang, C. W. Zhou, *Adv. Mater.*, 2003, **15**, 143.
4 P. C. Xu, Z. X. Cheng, Q. Y. Pan, J. Q. Xu, Q. Xiang, W. J. Yu, Y. L. Chu, *Sens. Actuators, B*, 2008, **130**, 802.
5 Z.W. Pan, Z. R. Dai, Z. L. Wang, *Science*, 2001, **291**, 1947.
6 M. Zhong, M. J. Zheng, L. Ma, Y. B. Li, *Nanotechnology*, 2007, **18**, 465605.
7 C. H. Liang, G. W. Meng, Y. Lei, F. Phillipp, L. D. Zhang, *Adv. Mater.*, 2001, **13**, 1330.
8 H. Q. Yang, R. G. Zhang, H. X. Dong, J. Yu, W. Y. Yang, D. C. Chen, *Cryst. Growth Des.*, 2008, **8**, 3154.
9 Z. B. Zhuang, Q. Peng, J. F. Liu, X. Wang, Y. D. Li, *Inorg. Chem.*, 2007, **46**, 5179.
10 P. Li, H.Q. Fan, Y. Cai, *Colloid Surf. A-Physicochem. Eng. Asp.*, 2014, **453**, 109.
11 P. Li, H.Q. Fan, *Mater. Sci. Semicond. Process.*, 2015, **29**, 83.
12 J.T. Zai, J. Zhu, R. R. Qi, X. F. Qian, *J. Mater. Chem. A*, 2013, **1**, 735.
13 H. Chen, Q. W. Wang, C. L. Kou, Y. M. Sui, Y. Zeng, F. Du, Sens. Actuators, B, 2014, **194**, 447.
14 Z. X. Cheng, L. Y. Song, X. H. Ren, Q. Zheng, J. Q. Xu, *Sens. Actuators, B*, 2013, **176**, 258.

15 P. Sun, W. Zhao, Y. Cao, Y. Guan, Y. F. Sun, G. Y. Lu, *CrystEngComm*, 2011, **13**, 3718.
16 C. C. Li, X. M. Yin, Q. H. Li, T. H. Wang, *CrystEngComm*, 2011, **13**, 1557.
17 H. R. Kim, K. I. Choi, J. H. Lee, S. A. Akbar, *Sens. Actuators, B*, 2009, **136**, 138.
18 C. X. Wang, L. W. Yin, L. Y. Zhang, Y. X. Qi, N. Lun, N. N. Liu, *Langmuir*,2010, **26**, 12841.
19 H. J. Zhang, R. F. Wu, Z. W. Chen, G. Liu, Z. N. Zhang and Z. Jiao, *CrystEngComm*, 2012, **14**, 1775.
20 Y. J. Chen, C. L. Zhu, X. L. Shi, M. S. Cao, H. B. Jin,*Nanotechnology*,2008,**19,** 205603.
21 A. Ponzoni, E. Comini, G.Sberveglieri, J. Zhou, S. Z. Deng, N. S. Xu, Y. Ding, Z. L. Wang, *Appl. Phys. Lett.*, 2006, **88**, 203101.
22 X. Q. Fu, J. Y. Liu, T. L. Han, X. M. Zhang, F. L. Meng, J. H. Liu, *Sens. Actuators,B*, 2013, **184**, 260.
23 R. D. Shannon, *Solid State Commun*., 1966, **4**, 629.
24 H. X. Dong, Z. H. Chen, L. X. Sun, L. Zhou, Y. J. Ling, C. Z. Yu, H. H. Tan, C. Jagadish, X. C. Shen, *J. Phys. Chem. C*, 2009, **113**,10511.
25 W. H.Zhang, W. D.Zhang, *J. Phys. Chem. Solids*, 2013, **74**, 1271.
26 Y. F.Sun, S. B.Liu, F. L.Meng, J. Y.Liu, Z.Jin, L. T.Kong, J. H. Liu, *Sensors*, 2012, **12**, 2610.
27 D. B. Yu, D. B. Wang, Y. T. Qian, J. *Solid State Chem*., 2004, **177**, 1230.
28 C. L. Chen, D. R. Chen, X. L. Jiao, C. Q. Wang,*Chem. Commun*., 2006, 4632.
29 S. E. Lin, W.C. Wei, *J. Am. Ceram. Soc*., 2006, **89**, 527.
30 S. F.Shokouh, P. V. Radovanovic, *J. Am. Chem. Soc.*, 2012,**134**,7015.
31 S. F.Shokouh, D.Neeshma, P. V. Radovanovic, *Chem. Mater*., 2010, **22**, 9.
32 C. T. Prewitt, R. D. Shannon,D. B. Rogers, A. W. Sleight, Inorg.Chem., 1969, **8**, 1985.
33 V. D, Ashok, S. K. De, *J. Phys. Chem. C*, 2011, **115**, 9382.
34 S. F.Shokouh, D.Neeshma, T.Wang, P. V. Radovanovic, *J. Phys. Chem. C*, 2009, **113**, 15928.
35 Y. Zhang, J. Q. Xu, Q. Xiang, H. Li, Q. Y. Pan, P. C. Xu, *J. Phys. Chem. C*, 2009, **113**, 3430.
36 N. Qin, X. H. Wang, Q. Xiang, J. Q. Xu, *Sens. Actuators, B*, 2014, **191**, 770.
37 X.C. Jiang, Y.L. Wang, T. Herricks, Y.N. Xia, *J. Mater. Chem*., 2004, **14**, 695.
38 T. T. Tseng, W. J. Tseng, *Ceram. Int*., 2009, **35**, 2837.
39 Q. Tang , W.J. Zhou , W. Zhang , S. M. Ou , K. Jiang , W. C. Yu , and Y. T. Qian, *Cryst. Growth Des*., 2005, **5**, 147.
40 J. Q. Xu, Y. P. Chen, Q. Y. Pan, Q. Xiang, Z. X. Cheng, X. W. Dong, *Nanotechnology*, 2007, **18**, 115615
41 M. Klaumünzer, M. Mačković, P. Ferstl, M. Voigt, E. Spiecker, B. Meyer, W. Peukert, *J. Phys. Chem. C*, 2012, **116**, 24529.
42 S. Avivi,Y. Mastai,A. Gedanken,*Chem. Mater*., 2000, **12**, 1229.
43 C. S. Prajapati, P. P. Sahay, *Sens. Actuators, B*,2011, **160**, 1043.
44 S. M. Wang, P. Wang, Z. F. Li, C. H. Xiao, B. X. Xiao, R. Zhao, T. Y. Yang and M.Z. Zhang, *New J. Chem*., 2014, **38**, 4879.
45 E. Li, Z. X. Cheng, J. Q. Xu, Q. Y. Pan, W. J. Yu, Y. L. Chu, *Cryst. Growth Des*., 2009, **9**, 2146.
46 X. M. Xu, X. Li, W. B. Wang, B. Wang, P. Sun, Y. F. Sun, G. Y. Lu, *RSC Adv*., 2014, **4**, 4831.
47 B.X. Li, Y. Xie, M. Jing, G. X. Rong, Y. C. Tang,, G. Z. Zhang, *Langmuir*, 2006, **22**, 9380.
48 D. Han, P. Song, H. H. Zhang, H. H. Yan, Q. Xu, Z. X. Yang , Q. Wang, *RSC Adv*. ,2014, **4**,50241.
49 N.Yamazoe, G. Sakai, K. Shimanoe, *Catal. Surv. Asia*, 2003, **7**, 63.
50 Y. S Li, J. Xu, J. F. Chao, D. Chen, S. X. Ouyang, J. H. Ye and G. Z. Shen, *J. Mater. Chem*., 2011, **21**, 12852.
51 A. S. Zuruzi, N. C. MacDonald,M. Moskovits and A. Kolmakov,*Angew. Chem., Int. Ed.*, 2007, **46**, 429 8.
52 T. Jinkawa, G. Sakai, J. Tamaki, N. Miura, N. Yamazoe, *J. Mol. Catal. A: Chem.*, 2000, **155**, 193.
53 H. Q. Cao, X. Q. Qiu, Y. Liang, Q. M. Zhu, M. J. Zhao, *Appl. Phys. Lett.*, 2003, **83**,761.
54 M. W. Ahn, K. S. Park, J. H. Heo, J. G. Park, D. W. Kim, K. J. Choi, J. H. Lee, S. H. Hong, *Appl. Phys. Lett*., 2008, **93**, 263103.
55 Y. Zeng, T. Zhang, L. J. Wang, and R. Wang, *J. Phys. Chem. C*, 2009, **113**, 3442.